



Retrieving soil surface roughness with the Hapke photometric model: Confrontation with the ground truth

S. Labarre^a, S. Jacquemoud^{a,*}, C. Ferrari^a, A. Delorme^a, A. Derrien^b, R. Grandin^a, M. Jalludin^c, F. Lemaître^d, M. Métois^e, M. Pierrot-Deseilligny^f, E. Rupnik^f, B. Tanguy^d

^a Institut de physique du globe de Paris - Sorbonne Paris Cité, Université Paris Diderot, UMR CNRS 7154, 1 rue Jussieu, 75005 Paris, France

^b Observatoire volcanologique du Piton de la Fournaise, Institut de physique du globe de Paris - Sorbonne Paris Cité, Université Paris Diderot, UMR CNRS 7154, 97418 La Plaine des Cafres, La Réunion, France

^c Centre d'étude et de recherche de Djibouti, BP 486, Djibouti, République de Djibouti

^d ONERA-DOTA - Université de Toulouse, 2 avenue Edouard Belin, BP 74025, 31055 Toulouse Cedex 4, France

^e Laboratoire de géologie de Lyon - Université Lyon 1, ENS de Lyon, UMR CNRS 5276, 69100 Villeurbanne, France

^f Laboratoire en sciences et technologies de l'information géographique - IGN, ENSG, Université Paris-Est, 94160 Saint-Mandé, France

ARTICLE INFO

Keywords:

Very high resolution digital elevation model
Surface roughness
Multiangular optical remote sensing
Field goniometer
Pleiades satellite
Hapke photometric model
Bayesian inversion
Asal-Ghoubbet rift

ABSTRACT

Surface roughness can be defined as the mean slope angle integrated over all scales from the grain size to the local topography. It controls the energy balance of bare soils, in particular the angular distribution of scattered and emitted radiation. This provides clues to understand the intimate structure and evolution of planetary surfaces over ages. In this article we investigate the capacity of the Hapke photometric model, the most widely used in planetary science, to retrieve surface roughness from multiangular reflectance data. Its performance is still a question at issue and we lack validation experiments comparing model retrievals with ground measurements. To address this issue and to show the potentials and limits of the Hapke model, we compare the mean slope angle determined from very high resolution digital elevation models of volcanic and sedimentary terrains sampled in the Asal-Ghoubbet rift (Republic of Djibouti), to the photometric roughness estimated by model inversion on multiangular reflectance data measured on the ground (Chamelon field goniometer) and from space (Pleiades images). The agreement is good on moderately rough surfaces, in the domain of validity of the Hapke model, and poor on others.

1. Introduction

Surface roughness, which can be understood as a measure of the topographic relief of bare soils, plays a key role in micrometeorology, hydrology, volcanology, geomorphology, planetary science and defense among others. It is a multiscale physical parameter which controls the energy balance, the scattering of incident radiation, and the directional emissivity of the ground, opening up the way for understanding the intimate structure and evolution of surfaces over ages. Multiangular optical imagery is commonly used in planetary science to remotely provide a valuable information about roughness, a physical characteristic of soils that generates shadows at all scales. It is incorporated in photometric models through a shadowing function, with varying complexity. This function can be itself related to different characteristics of

the boundary surface: ratio of mean hole depth-to-radius (Lumme and Howell, 1981), mean slope angle of all the facets (Hapke, 1984), or fractal dimension (Shkuratov and Helfenstein, 2001). From a radiometric perspective, the shadowing function partly drives the shape of soil BRDF (Bidirectional Reflectance Factor; Schaepman-Strub et al., 2006). However, the validation of these models on planetary bodies is indirect.

Models using other shadowing functions have been assessed on terrestrial surfaces (e.g., Cierniewski, 1987; Irons et al., 1992; Despan et al., 1999) but most of them have been validated only in the lab or in the field. All this work has opened up new perspectives to probe soil physical properties in the solar domain. On Earth, field measurements of surface roughness are pricy, difficult to implement and inefficient to cover large areas. Photogrammetric techniques now provide low-cost

* Corresponding author.

E-mail addresses: labarre@ipgp.fr (S. Labarre), jacquemoud@ipgp.fr (S. Jacquemoud), ferrari@ipgp.fr (C. Ferrari), delorme@ipgp.fr (A. Delorme), derrien@ipgp.fr (A. Derrien), grandin@ipgp.fr (R. Grandin), mohamed.jalludin@gmail.com (M. Jalludin), francois.lemaitre@onera.fr (F. Lemaître), marianne.metois@univ-lyon1.fr (M. Métois), marc.pierrot-deseilligny@ensg.eu (M. Pierrot-Deseilligny), ewelina.rupnik@ensg.eu (E. Rupnik), bernard.tanguy@onera.fr (B. Tanguy).

<https://doi.org/10.1016/j.rse.2019.02.014>

Received 22 June 2018; Received in revised form 25 January 2019; Accepted 17 February 2019

0034-4257/ © 2019 Elsevier Inc. All rights reserved.

high-resolution surface topographic models, from which various statistical parameters can be derived (e.g., Bretar et al., 2013; Gilliot et al., 2017). Remote sensing allows investigation of large or inaccessible areas. Nonetheless scientists are still looking for a robust method to derive surface roughness. For instance the interpretation of radar images ensuing from the direct link between the backscattering coefficient and roughness remains relatively tricky. LiDAR is also a powerful tool for analyzing soil topography but generally limited to the topographic scale.

To date the Hapke model is the most widely used photometric model in the scientific community (Hapke, 2012). Although it gave rise to many improvements over the last thirty years, in particular with regard to the physics of light-matter interaction, its formulation and the significance of its input parameters are still debated. Nevertheless this model is simple and reproduces well the photometric response of bare surfaces measured in the laboratory (e.g., Jacquemoud et al., 1992; Chappell et al., 2006; Shepard and Helfenstein, 2007, 2011; Souchon et al., 2011; Beck et al., 2012; Pommerol et al., 2013; Johnson et al., 2013), in the field (e.g., Pinty et al., 1989; Johnson et al., 2006a, 2006b) or from space (e.g., Wu et al., 2009; Ceamanos et al., 2013; Fernando et al., 2013; Vincendon, 2013; Sato et al., 2014). To what extent multiangular imagery can inform us about soil roughness is, however, still a pending question. The validation of the Hapke model, i.e., the comparison of the retrieved parameters with the ground truth, still requires effort. Multiangular earth-orbiting satellites (e.g., MISR, Pleiades, POLDER, Proba-1, SkySat) are designed to sample the directional reflectance over bare soils at various spatial and spectral resolutions in the visible and near-infrared wavelengths. However, due to the scarcity of concomitant in situ surface roughness and radiometric measurements, their ability to retrieve soil roughness has not been demonstrated so far.

This article aims at estimating surface roughness on bare soils using the Hapke model from both field and orbital photometric data, and to compare the retrieved values with in situ measurements acquired in the Asal-Ghoubbet rift (Republic of Djibouti). First, we present the study site and in situ measurements (Section 2). Next, we expose the Pleiades satellite data after atmospheric correction and cross calibration with field data (Section 3). A Bayesian inversion of the Hapke model is performed on both field and satellite data to estimate the photometric roughness of 12 sites and discuss the coherence between the retrieved values (Section 4). Finally, a discussion of the results is provided (Section 5).

2. Field data

2.1. Study site

The Asal-Ghoubbet rift (Republic of Djibouti) is a young active rift. It began to form 900,000 years ago by extending the Somalia-Saudi plate boundary from the oceanic domain towards the west, to the triple point of Africa-Arabia-Somalia, currently located within the depression of Afar. It has been the subject of many research works in geophysics since the early 1970s because it allows small-scale study of the oceanic accretion above sea level (Fig. 1).

This unique site meets the objectives of our study for two reasons:

- 1) it displays a wide variety of bare soils over a small area ($\sim 100 \text{ km}^2$), from pure white salt deposits to dark lava basalt flows, a contrasted topography, and a great wealth of surfaces, from very rough lava flows to flat deposits in sedimentary basins (Fig. 2);
- 2) it has a desert climate so that soils are marginally wet and sparsely vegetated. Because of the presence of shoreline terraces generated during the formation of the rift, the lands are generally homogeneous and flat.

A first exploratory mission has been conducted in April 2015 to

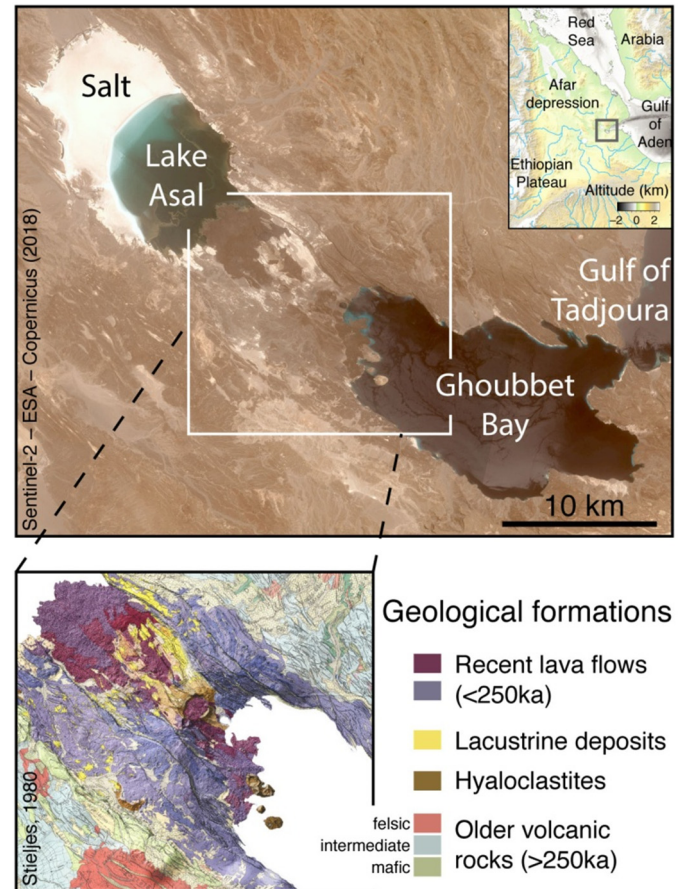


Fig. 1. Geographic context of the study site ($11^{\circ}35'N$, $42^{\circ}29'E$). The image on top is a Sentinel-2 image of the Asal-Ghoubbet rift, Republic of Djibouti, acquired on 26 May 2018. The main water bodies and recent lava flows can be distinguished by their darker color, whereas recent sedimentary deposits (including salt deposits) have a brighter aspect. The bottom panel is a simplified geological map of the main area of interest targeted in this study (Stieltjes, 1980, modified from Pinzuti et al., 2013).

identify areas of interest, and the main campaign took place for two weeks in February 2016. Although organizing a field trip in this rift is a challenge (desert area, strong winds, rudimentary infrastructure), it is easily accessible by car, which makes it an ideal playground for our study.

2.2. In situ roughness measurement

In order to determine the roughness parameter from the slope distribution of these terrains, the topography has been reconstructed at the millimeter scale by means of UAV imaging.

2.2.1. Topographic reconstruction at millimeter scale

Twenty two sites spanning over $30 \text{ m} \times 40 \text{ m}$ areas have been surveyed using a quadcopter (DJI F450) equipped with a flight control system, a compact-system camera (Sony Alpha 5100) and an interchangeable lens (Sigma 30 mm F2.8). The quadcopter was maintained at a flight altitude between 8 m and 15 m to obtain a pixel size on the ground ranging from 1 to 2 mm. In this windswept region, the camera settings (i.e., exposure time, aperture, and sensitivity) were adapted to each site so as to provide correct image exposure. A camera calibration was also performed in the vicinity of the survey area for maximum precision in the digital elevation model (DEM) reconstruction phase. To realize it, a set of convergent images of a three-dimensional scene (rocks, buildings, etc.) was taken by hand prior to each UAV

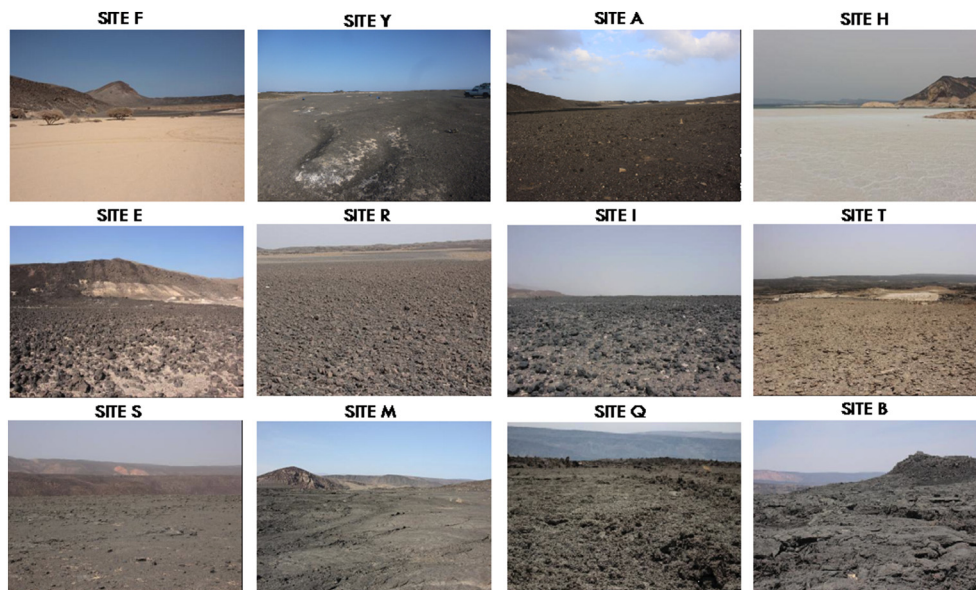


Fig. 2. Twelve surfaces of increasing roughness studied in the Asal-Ghoubbet rift. From top left to bottom right, clay deposits (site F); reshaped hyaloclastic projections (site Y); lapilli deposits (site A); salt bank (site H); centimetric lava blocks (hyaloclastite) on lacustrine deposits (site E); slag on lacustrine deposits (site R); decimetric lava blocs on lacustrine deposits (site I); pulverulent limestone, rich in mollusc shells (site T); altered aphyric lava (site S); cracked lava crust (site M); basalt porphyry lava in the form of slabs (site Q); ropy pahoehoe lava (site B). See Caminiti (2000) for more information about the geomorphology of the rift.

acquisition.

The quadcopter was flown by an operator along parallel lines above the surface. Flight height and path were controlled by real-time GNSS feedback on the aircraft position. An image overlap of 80% along the flight line and of 50% across the flight line was achieved by controlling the camera automatic shooting time interval, the UAV speed and the trajectory. To geo-reference the images, five ground control points designed to be easily identified in the UAV images were distributed symmetrically across each measured site, and their geographical coordinates were measured with dual-frequency GPS receivers (Ashtech Z-X) and their antennas (Ashtech Geodetic 4) at 1 Hz sampling frequency. The accuracy of the position of these targets was estimated at approximately 1 ± 0.7 cm (latitude), 0.4 ± 0.3 cm (longitude) and 1.3 ± 1.1 cm (altitude). In addition, wooden pieces of defined dimensions ($150 \text{ mm} \times 35 \text{ mm} \times 35 \text{ mm}$) were spread in the fields to provide three-dimensional control information for a posteriori DEM validation.

The workflow to reconstruct the high resolution topography follows the steps described by Bretar et al. (2013). It is based on MicMac, an open-source photogrammetric software (<https://micmac.engg.fr/>) (Pierrot-Deseilligny and Paparoditis, 2006; Rupnik et al., 2017). Only 12 out of 22 sites (A, B, E, F, H, I, M, Q, R, S, T and Y) have been processed to date on various reasons including wrong internal calibrations, overlapping problems, and time constraints. The spatial resolution of the DEMs ranges from 2.5 mm to 4 mm. Fig. 3 displays the shaded relief of four contrasted sites presented in Fig. 2. The planimetric accuracy is of the order of a few millimeters, while the relative vertical positional errors on the wooden pieces mentioned above are $< 3\%$.

2.2.2. Surface roughness determination

The mean roughness parameter $\bar{\theta}$ was computed using Eq. (1) (Labarre et al., 2017).

$$\tan \bar{\theta} = \frac{2}{\pi} \int_0^{\pi/2} a(\theta) \tan \theta d\theta \quad (1)$$

with θ the slope angle of each facet of the surface and $a(\theta)$ the slope angle distribution. In order to compare the roughness between sites, a square 20 m on a side was extracted from each DEM and decomposed into twenty-five squares 4 m on a side to facilitate computations. The mean and the standard deviation of $\bar{\theta}$ calculated for the 12 sites are given in Table 1 and the slope distributions are illustrated in Fig. 4. The slopes of the two smoothest sites, F and Y, are $< 50^\circ$. Sites E and R

show similar distributions. The distributions of sites B and Q reveal very few values $> 70^\circ$ because they present little discontinuities. Sites M and S have the same roughness and similar distributions, except that the amplitude at angles $> 50^\circ$ is stronger for site S due to the presence of pebbles and centimeter blocks on the surface. The roughness of sites B, A and Y is comparable to that found in the Piton de La Fournaise for similar terrains (Bretar et al., 2013; Labarre et al., 2017).

2.3. In situ multiangular photometric measurements

In order to estimate the photometric roughness with the Hapke model at microscopic and mesoscopic scales, the bidirectional and spectral radiances were measured in the field over 10 of the selected soils (A, D, E, F, H, M, O, Q, R, and T) with the Chamelon, a new portable field goniometer system designed by ONERA (Toulouse, France) to record the hemispherical conical reflectance factor and coupled with a FieldSpec 4 spectroradiometer (ASD Inc.). They are both remotely controlled by an in-house developed software and mounted on a cart equipped with wheels to facilitate movement. Such outdoor measurements that developed in recent years are still challenging (e.g., Sandmeier, 2000; Doctor et al., 2015; Bachmann et al., 2016; Furey, 2016; Harms et al., 2016). The remoteness of the Asal-Ghoubbet rift, strong winds and high temperatures during the field experiment made things even more difficult.

A four-axis articulated arm allowed to perform directional measurements. The radiance of each targetted field was measured using a fixed 8° instantaneous field-of-view (IFOV): this corresponds to a disk of about 20.56 cm in diameter at nadir, assuming a conical view and a distance to the target of 147 cm. This footprint changes to an ellipse with increasing viewing angle: it is four time bigger at a 60° viewing angle. The measurements are made according to the following protocol (Fig. 5): the Chamelon is facing the sun; the solar zenith angle is calculated knowing the Julian day, the universal time, the latitude and longitude of the site; the articulated arm moves in five measurement planes: two principal planes of the Sun (left and right side), one perpendicular plane, and two 45° planes (left and right side). The radiance of the ground is acquired in thirteen viewing directions from -59.11° to $+59.09^\circ$ in each of the five planes, and in-between, the radiance of a Spectralon reference panel (Labsphere) is acquired at nadir. At the end of an acquisition cycle, the arm circularly moves around the device to sample the surface at nadir. A complete cycle thus represents 103 measurements: 7 vertical measurements on the Spectralon panel, 5×13 directional measurements and $15 + 16$ vertical measurements.

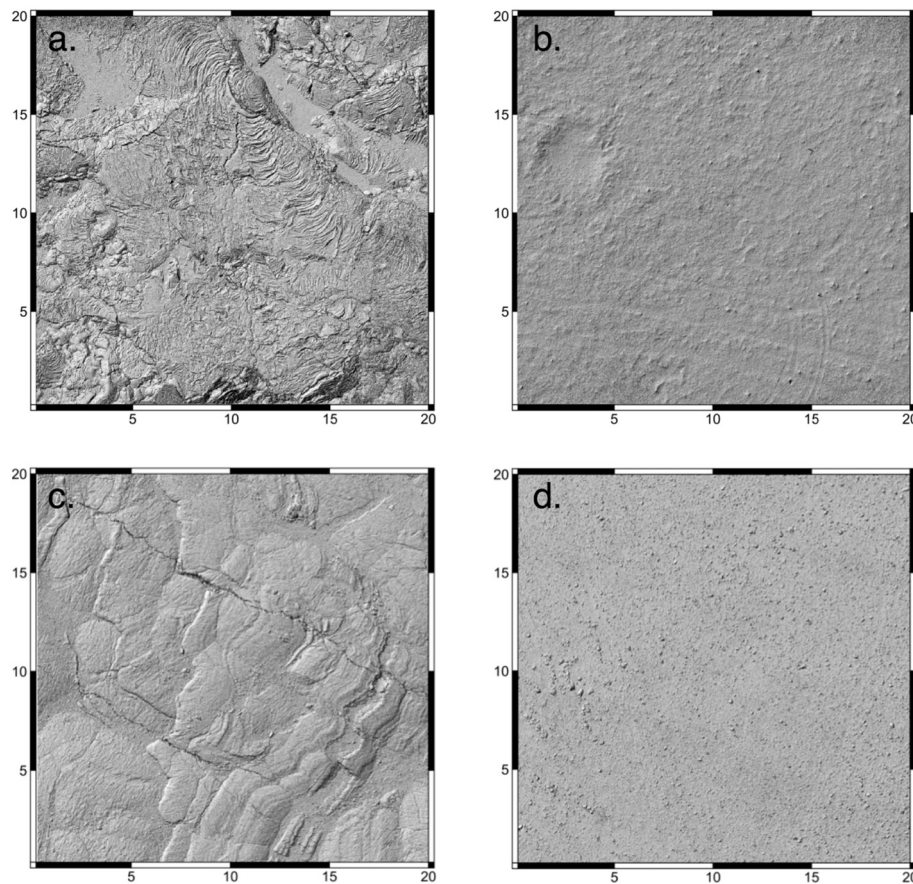


Fig. 3. 20 m long-sided areas extracted from shaded relief maps of digital elevation models for four remarkable sites of the Asal-Ghoubbet rift: sites (a) B, (b) F, (c) M, and (d) R. The spatial resolution of these four DEMs ranges from 2.8 mm to 3.2 mm.

A cycle approximately lasts 17 min whereas the sun zenith and azimuth angles are likely to vary from 0.43° to 4.81° and from 0.83° to 9.32° , respectively, depending on the time of the day. Variations in sun zenith angle are more important early in the morning and late in the afternoon. Conversely, variations in solar azimuthal angle are maximum around noon. Such variations are not inconvenient for the inversion of the Hapke model, because the illumination and viewing angles are exactly known for each measurement.

In order to appraise the spatial variability of the bidirectional reflectance factor, between two and six positions were sampled within each site by moving the Chamelon a few meters. For portability reasons, and since the size of the smallest area measured on the ground must be statistically representative of the site, the rougher terrains have not been measured.

Table 1

Geographical coordinates, geological description, mean roughness ($\bar{\theta}$) and standard deviation (SD) of 12 sites. The values of $\bar{\theta}$ and SD expressed in degrees are calculated over 25 tiles of 16 m^2 each.

Site	Latitude N	Longitude E	Description	$\bar{\theta}$	SD
A	11.5810209904	42.4930719598	Lapilli deposits	18.6	± 2.1
B	11.5945984130	42.4726550328	Ropy pahoehoe lava	33.4	± 5.1
E	11.5936487248	42.4917893931	Centimetric lava blocks (hyaloclastite) on lacustrine deposits	23.1	± 2.9
F	11.5925120813	42.4958721760	Clay deposits	8.3	± 1.7
H	11.6199221528	42.3965061773	Salt bank	20.9	± 2.2
I	11.5633683315	42.4485707122	Decimetric lava blocs on lacustrine deposits	27.9	± 2.4
M	11.5896442760	42.5030110060	Cracked lava crust	18.3	± 1.9
Q	11.5618838898	42.5136321246	Basalt porphyry lava in the form of slabs	33.1	± 4.2
R	11.5361663318	42.4923411655	Slag on lacustrine deposits	23.1	± 1.3
S	11.5416993639	42.4811000172	Altered aphyric lava	18.3	± 2.6
T	11.5585832484	42.4558691802	Pulverulent limestone, rich in mollusc shells	20.9	± 2.6
Y	11.5864054883	42.4881465853	Reshaped hyaloclastic projections	12.6	± 2.0

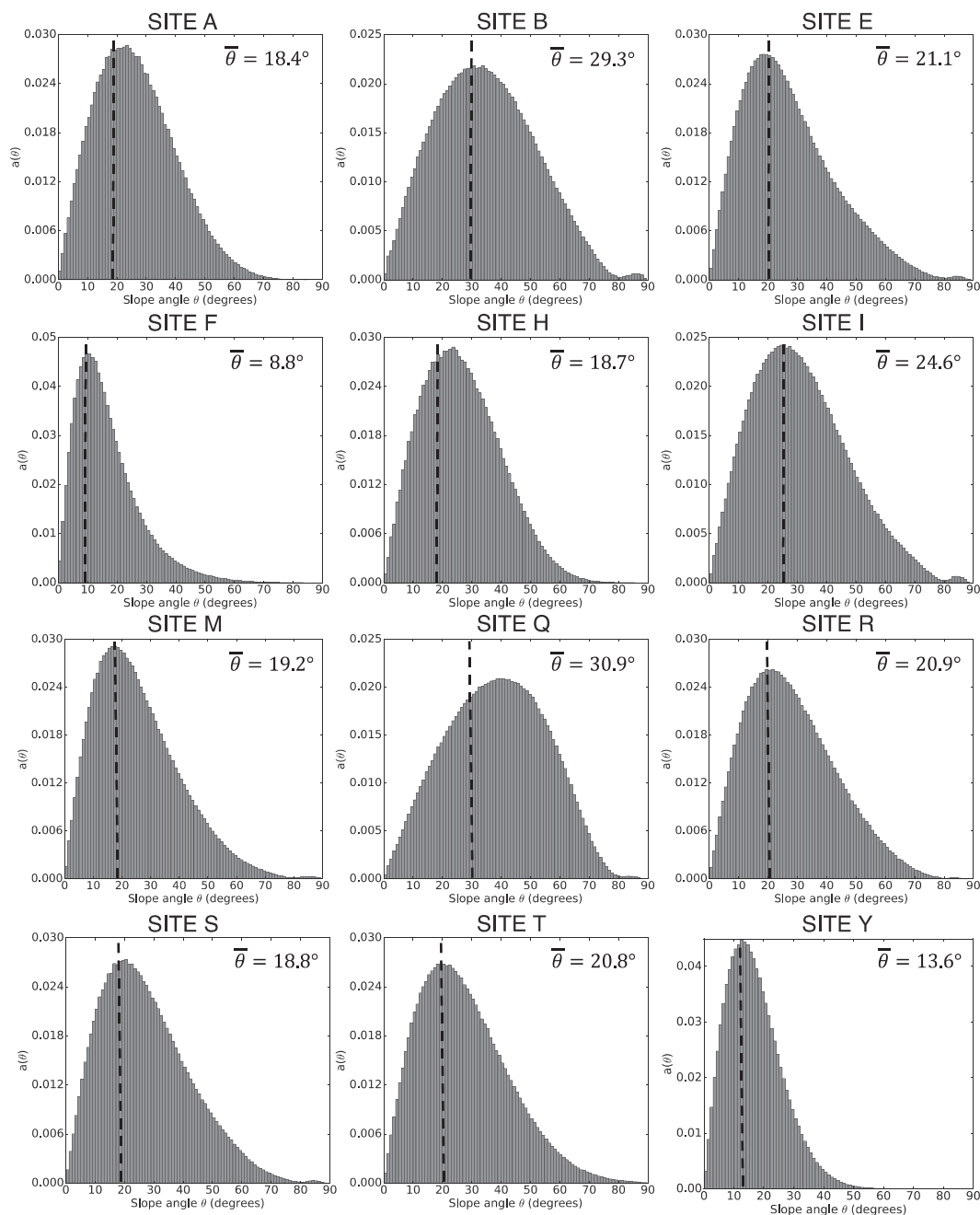


Fig. 4. Slope distribution evaluated on one tile representative of the twelve sites introduced in Fig. 2. The dashed lines correspond to the roughness values $\bar{\theta}$ determined using Eq. (1). Note that the values indicated in each panel are slightly different from those displayed in Table 1, which are averages of 25 tiles.

reflectance measured between the directions 13 and 14.

3. Satellite data

The agility of the Pleiades satellite allows unique measurements of the ground BRF at macroscopic scale. A sensitivity analysis demonstrates the impact of the aerosol optical thickness on the observed BRF. Cross-calibration with the Chamelon data improves the atmospheric correction by fixing the other important factor impacting the correction, i.e., the adjacency radius.

3.1. Pleiades images

The Pleiades 1A and 1B satellites, launched in December 2011 and December 2012, operate on the same quasi-circular orbit at an altitude

of 694 km and they are 180° out of phase. They aim to image the surface of the Earth in the visible-near infrared wavelengths with both a 50 cm spatial resolution in panchromatic mode and a 2 m spatial resolution in multispectral mode (blue, green, red, and near infrared) (Fig. 7c). In addition to a high spatial resolution, they offer exceptional agility that allows rapid off-nadir acquisitions up to ~50°, thus offering many different observation geometries (Gleyzes et al., 2012; Lachéradé et al., 2012). One can take advantage of this property to produce high resolution DEMs (Rupnik et al., 2018). During the in-orbit commissioning phase of the Pleiades 1B satellite conducted by CNES (Centre national d'études spatiales), a series of twenty-one multiangular images were acquired in video mode in a single flyby of the Asal-Ghoubbet rift on January 26, 2013 (Fig. 7a, b). The total acquisition time was about 4 min, from 7:49:18 UTC to 7:53:27 UTC. The swath along the orbital track varied from ~20 km at nadir to ~60 km at grazing angle. The

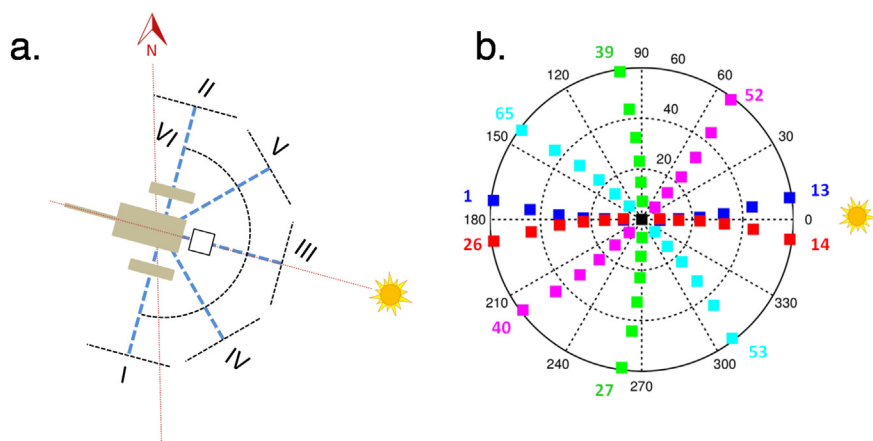


Fig. 5. (a) Measuring planes of the Chamelon field spectro-goniometer: (I) right principal plane of the Sun, (II) left principal plane of the Sun, (III) perpendicular plane, (IV) oblique plane at 45° azimuth on the right, (V) oblique plane at 45° azimuth on the left, and (VI) circular sight. (b) Sampled viewing directions: main plane on the right (blue), main plane on the left (red), perpendicular plane (green), oblique plane at 45° azimuth on the right (magenta), oblique plane at 45° azimuth on the left (cyan). The numbers from 1 to 65 indicate the order of the directional measurements. (For interpretation of the references to color in this figure legend, the reader is referred to the web version of this article.)

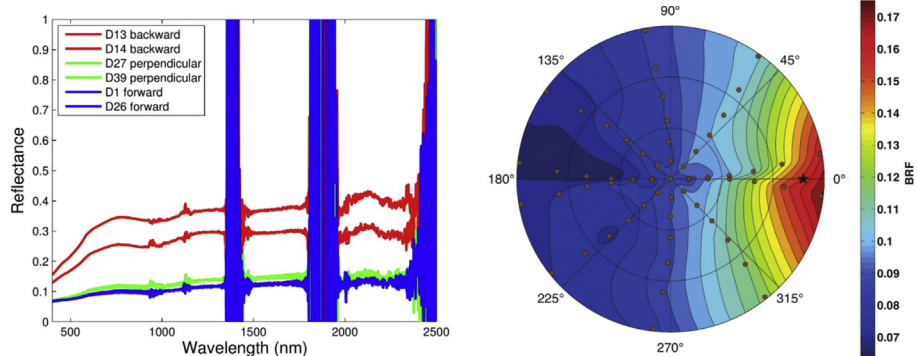


Fig. 6. (left) Reflectance spectra of site A for six viewing directions as described in Fig. 5a. The noisy values around 1400 nm, 1900 nm, and 2500 nm are located in spectral regions where atmospheric water vapor strongly absorbs radiation. (right) Bidirectional reflectance factor of site A averaged over the panchromatic band of Pleiades (see Fig. 7c).

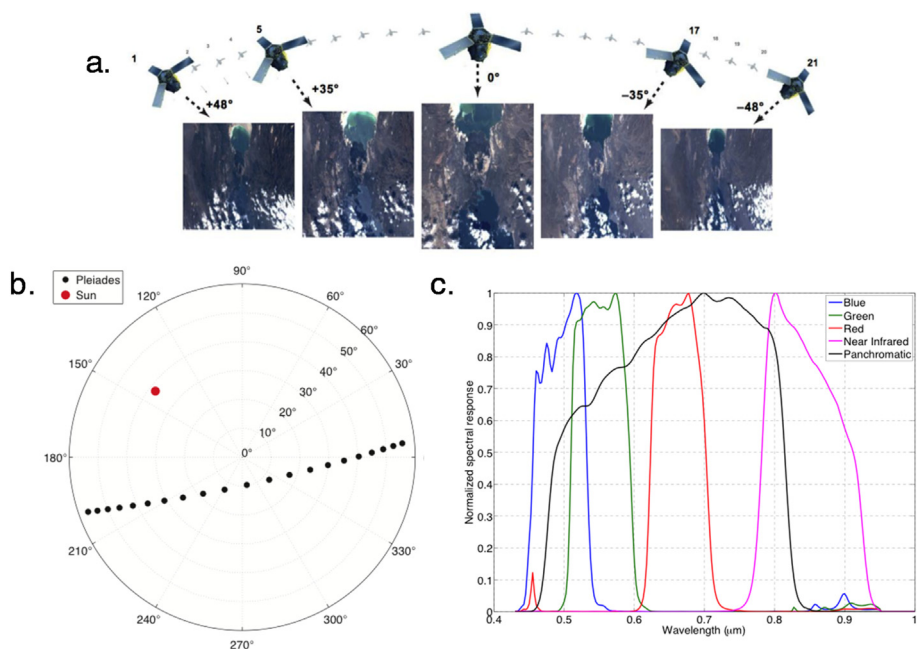


Fig. 7. (a) Visual representation of the Pleiades video acquisition; (b) Observing geometry of the studied zone: the black dots indicate the viewing directions and the red disk the position of the Sun in an azimuth-elevation projection; (c) Normalized spectral bands of the Pleiades satellite (Lachérade et al., 2012). (For interpretation of the references to color in this figure legend, the reader is referred to the web version of this article.)

high resolution multi-angular reflectances acquired with a large angular sampling over a wide range of surfaces in terms of color, roughness and mineralogical properties, is unique.

3.2. Atmospheric corrections

The atmospheric correction of the 21 Pleiades images is a critical step impacting the shape of the BRF, therefore the accuracy of the

retrieved surface roughness. It is based on the 6S radiative transfer code (Vermeete et al., 1997) which is implemented in the Orfeo ToolBox library (OTB, <https://www.orfeo-toolbox.org/>), a set of algorithmic bricks and satellite image processing utilities developed by CNES and designed to process the Pleiades images (Fig. 8). Four atmospheric parameters have to be provided using ancillary datasets: the atmospheric pressure P_a , the water vapor content U_{H_2O} , the ozone content U_{O_3} , and the aerosol optical thickness τ_A . They were all determined over

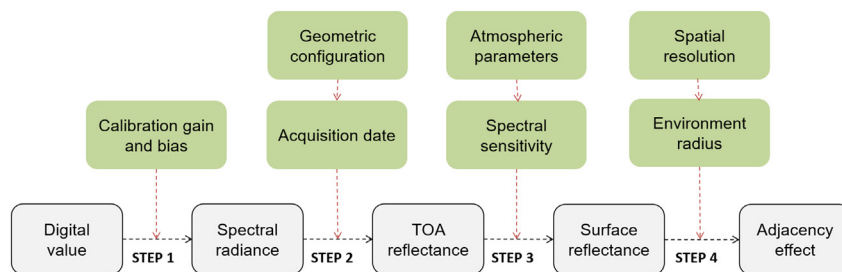


Fig. 8. Orfeo ToolBox (OTB) processing chain for radiometric calibration of the Pleiades images. The white frames represent the steps and the green frames the input parameters. (For interpretation of the references to color in this figure legend, the reader is referred to the web version of this article.)

Djibouti on January 26, 2013.

Atmospheric pressure and ozone content do not vary much spatially and temporally, so they can be estimated from low spatial resolution meteorological data. On the contrary, water vapor and aerosol content are highly variable so the calibration requires data with high temporal and spatial resolution. In the absence of atmospheric measurements at the satellite flew over the Asal-Ghoubbet rift, the aerosol optical thickness was provided by the MODIS (*Moderate Resolution Imaging Spectrometer*) instrument onboard the AQUA satellite: $\tau_A = 0.22$. The water vapor content was also derived from the MODIS instrument onboard the TERRA satellite: $U_{H_2O} = 2.325 \text{ g} \cdot \text{cm}^{-2}$. The column ozone content has been derived from the OMI (*Ozone Monitoring Instrument*) spectrophotometer onboard the AURA satellite: $U_{O_3} = 244 \text{ DU}$. Finally, the Global Modeling and Assimilation Office that supports NASA's Earth Science mission uses the GEOS-5 atmospheric data assimilation model to build a consistent temporal database for sea level atmospheric pressure: $P_a = 1014.72 \text{ hPa}$.

The 6S code computes four radiometric quantities in the solar domain between 400 nm and 2500 nm: the intrinsic reflectance and the spherical albedo of the atmosphere, the total gaseous transmission, and the total transmittance of the atmosphere along both the sun-surface and surface-satellite optical paths. To take into account the adjacency effect, the average reflectance from contiguous pixels within a circle of radius r around the target pixel is calculated and a correction is made (Appendix A). The processing chain leading to the surface reflectance of the region of interest is applied to the 21 images separately, and the region of interest is then projected onto each sensor geometry as a polygon. The bidirectional reflectance value at a given viewing angle is the mean value of the pixels included in the resulting polygon and the error is the confidence interval at 95%.

3.3. Sensitivity of bidirectional reflectance to atmospheric parameters

As mentioned earlier, the shape of the BRF is of critical importance to the retrieval of accurate surface roughnesses. In order to quantify the impact of atmospheric corrections on the calculation of surface reflectance, a one-factor-at-a-time sensitivity analysis of the atmospheric parameters was carried out on two zones selected on criteria of color and roughness (Fig. 9): zone 1 is a silty, flat and bright surface while zone 2 is basalt, rough and dark lava flow. The reflectance factor is first calculated at ground level using the default parameter set implemented in the OTB: $U_{O_3} = 0 \text{ DU}$, $U_{H_2O} = 2.5 \text{ g} \cdot \text{cm}^{-2}$, $P_a = 1030 \text{ hPa}$, $\tau_A = 0.2$, desert aerosol model, and no adjacency effect correction.

The effect of water vapor is limited to a modulation of the amplitude of the reflectance. It is reduced in the visible with variations $< 5\%$, and notable in the near infrared beyond 700 nm due to the presence of weak absorption bands. The ozone content has a larger impact in the visible, in particular in the green band of Pleiades covering the Chappuis band between 550 nm and 650 nm, and has no effect in the near infrared. The influence is important at grazing angles, which results in a significant deformation of the multi-angular reflectance. The atmospheric pressure has a relative impact of $< 5\%$. Like water vapor, it acts as a scaling

factor and is not critical to the correction of the reflectance. Conversely, one can observe a strong influence of aerosol optical thickness on the shape of the reflectance distribution, especially in zone 2 which is darker. The difference with the reference distribution can reach 100% for extreme values, and it tends to increase with the viewing angle or towards shorter wavelengths. Finally, extending the adjacency radius changes both the amplitude and the shape of the reflectance distribution. Therefore, the two most influential atmospheric parameters critical for the determination of soil roughness are the aerosol optical thickness and the adjacency radius.

3.4. Cross-calibration between Pleiades and Chamelon measurements

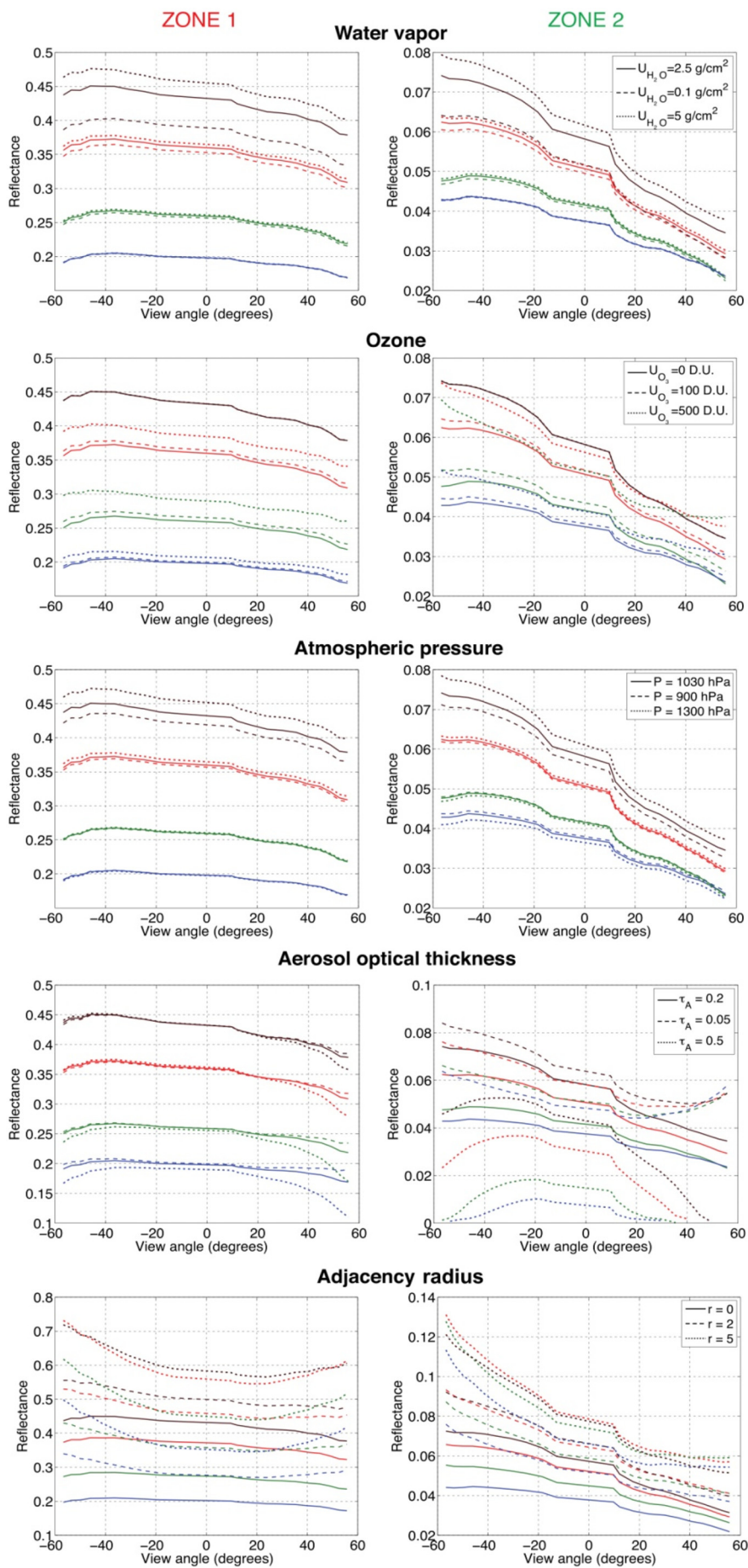
In situ measurements conducted in the Asal-Ghoubbet rift were used as ground truth to check and to adjust the quality of the orbital measurements. We superimposed the Pleiades reflectances acquired in four spectral bands and at 21 viewing angles on the Chamelon reflectances acquired from 400 nm to 900 nm and at 65 viewing angles. Fig. 10 displays the reflectance factor ratio relative to the green band, chosen arbitrarily, for sites F (clay deposits), M (decimetric lava blocs on crust), and T (pulverulent limestone) and two adjacency radii ($r = 0$ and $r = 1$). The agreement is best when $r = 1$ so we used this value to extract the photometric curves of the Pleiades images. On applying this correction the reflectance as derived from Pleiades tends to decrease in the near infrared down to a lower value than in the red (Fig. 10). This effect is greater for site M, the spectral signature of which is typical of lunar basalts (e.g., Staid, 2000; Antonenko and Osinki, 2010).

3.5. Pleiades multiangular reflectance

Fig. 11 illustrates the bidirectional reflectance factor (BRF) extracted over 12 sites in the four spectral bands of the Pleiades satellite after calibration. The average albedo of sites F (clay deposits), T (pulverulent limestone) and H (salt bank) changes from bright to very bright. The shape of the BRF versus the viewing angle of site H is slightly convex, whereas that of site F is flat and collapses at grazing viewing angles. Site T exhibits a negative slope. The shape and magnitude of the BRF of the other sites are similar in the four spectral bands, except at site R for which some points are missing due to the presence of clouds and shadows, and sites B and Q that display lower amplitude. The BRF of sites A, S and Y is similar despite different surface features. The roughest surfaces of sites B and Q are also comparable. At first glance, one can note that the Pleiades BRF does not vary much in shape and that the albedo seems to be a more robust segmentation criterion.

4. Results on soil roughness

In this section we examine whether the mean surface roughness derived from very high resolution DEMs is consistent with the photometric roughness retrieved by inversion of the Hapke model on soil multiangular reflectance data acquired at centimeter and meter scales.



(caption on next page)

Fig. 9. Determination of the bidirectional reflectance factor (BRF) of two contrasted zones (left/right) in the four Pleiades bands (R: red lines, G: green lines, B: blue lines, PIR: black lines) along the acquisition geometry (Fig. 3) for the default parameters set (solid line) and high (dotted line) and low (dashed line) values of the parameters of the atmospheric correction. The adjacency radius r is expressed in pixel. (For interpretation of the references to color in this figure legend, the reader is referred to the web version of this article.)

4.1. The Hapke model

The bidirectional reflectance factor of a particulate medium can be calculated using the radiative transfer model developed by Hapke (1981). The latest version that considers the porosity correction is written as (Hapke, 2008):

$$\pi r_R(i, e, g) = \frac{K(P) w \mu_{0e}}{\mu_0 \ 4 \ \mu_{0e} + \mu_e} (p(g, b, c) B_S(B_0, P, g) + M(w, \mu_{0e}, \mu_e) S(i, e, g, \bar{\theta}_H)) \quad (2)$$

with $K(P)$ the porosity coefficient related to the porosity P of the medium, w the single-scattering coefficient (ratio of scattering coefficient to total extinction coefficient), i and e the illumination and viewing angles, respectively ($\mu_0 = \cos i$ and $\mu = \cos e$), $p(g, b, c)$ the phase function for the phase angle g and the phase function parameters b (anisotropy parameter) and c (backscattering coefficient), B_S the function describing the shadow-hiding opposition effect (SHOE) and depending on the parameter B_0 , named opposition surge amplitude, M a function modeling multiple scattering, and S a shadowing function quantifying the effects of the photometric roughness $\bar{\theta}_H$ (Appendix B). μ_{0e} and μ_e are the cosines of the effective illumination and viewing angles, the expressions of which depend on $\bar{\theta}_H$.

4.2. Photometric roughness

Many authors have inverted the Hapke model by using conventional non-linear least squares methods (e.g., Jacquemoud et al., 1992; Gunderson et al., 2006; Shepard and Helfenstein, 2007; Wu et al., 2009; Helfenstein and Shepard, 2011) but the parameter uncertainties have been seldom, if ever, determined. Fernando et al. (2015) and Schmidt and Fernando (2015) recently demonstrated the relevance of a probabilistic inversion to estimate the photometric parameters of the model over Mars. We followed their approach on the Pleiades and Chamelon reflectances.

The complete Hapke model depends on six parameters (w , $\bar{\theta}_H$, B_0 , P , b and c) for which no prior information is available. A uniform probability density function (PDF) is thus considered over their range of variation. Outside this range, the PDF equals zero to discard

nonphysical solutions. A global sensitivity analysis of the model performed by Labarre et al. (2017) confirmed that the opposition surge amplitude B_0 did not influence the estimation of the other parameters, which was suspected by other authors (e.g., Wu et al., 2009; Fernando et al., 2013). However we left it free during the inversion insofar as the calculation time was not significantly affected. The inversion of the model was performed using the Python PyMC library (Patil, 2010) that implements Bayesian statistical models and fitting algorithms, including Markov Chains Monte Carlo. The retrieved values of the parameters are the median of the a posteriori PDF provided by PyMC, and the uncertainties corresponds to the 95% confidence interval. The inversion is a two-stage process: first synthetic tests are carried out in different geometrical configurations; second the model is inverted on the Pleiades and Chamelon data. Only three parameters are likely to be accurately constrained by inversion from the observations: w , $\bar{\theta}_H$ and b .

Since the grain size is assumed to be larger than the wavelength (a major hypothesis of the model), the roughness and the phase function parameters are assumed to be wavelength independent. Same with the porosity and the opposition effect parameter, the influence of which on the model is small. Therefore, the single scattering albedo, which is related to the optical constants of the constituting materials of the medium, is the only wavelength-dependent parameter. Because of the interactions between w and some parameters (Labarre et al., 2017), their estimated values may vary with wavelength, although this is physically meaningless.

The inversion of the Hapke model was first conducted both on the spectral (R, G, B and NIR) and the panchromatic (P) bands of Pleiades. In total 21 viewing angles were available for the 12 sites except for site R where the number of observations was reduced to 13 due to the presence of clouds in some images. Although the preliminary tests revealed a deterioration in the estimation of the photometric parameters as the number of observations decreased, the constraint on the parameters remained good on this site. Assuming that only w varies spectrally, we also inverted the model on the four spectral bands simultaneously, as suggested by Jacquemoud et al. (1992), Chappell et al. (2006) and Wu et al. (2009). This led to the retrieval of 9 parameters: the four single scattering albedos (w_R , w_G , w_B and w_{NIR}), the photometric roughness ($\bar{\theta}_H$), the two phase function parameters (b and c), the

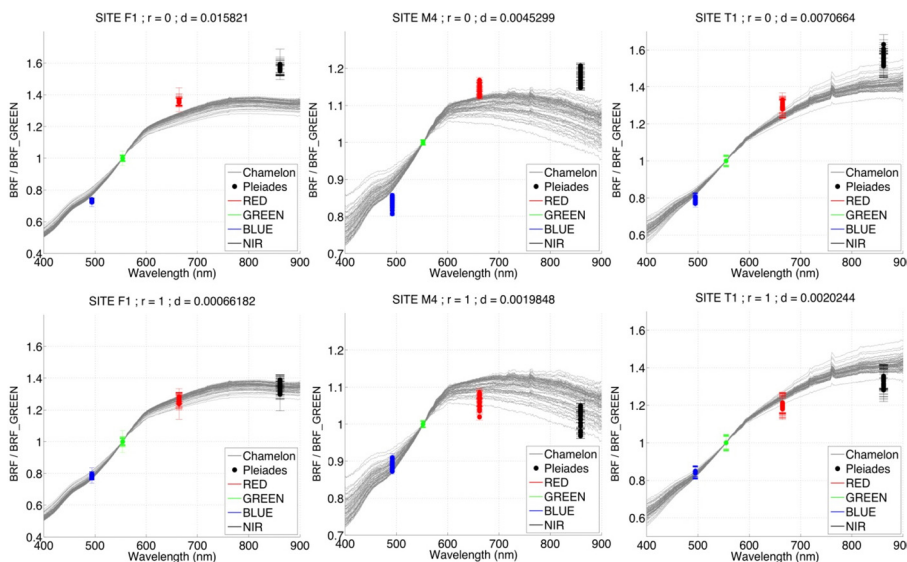


Fig. 10. Comparison between the ratio to the green band of the bidirectional reflectance factor (BRF) spectra for the Chamelon (gray curves) and Pleiades (colored dots) for different values of the adjacency effect radius ($r = 0$ at the top; $r = 1$ at the bottom) and for the sites F (left), M (middle) and T (right) of the Asal-Ghoubbet rift. (For interpretation of the references to color in this figure legend, the reader is referred to the web version of this article.)

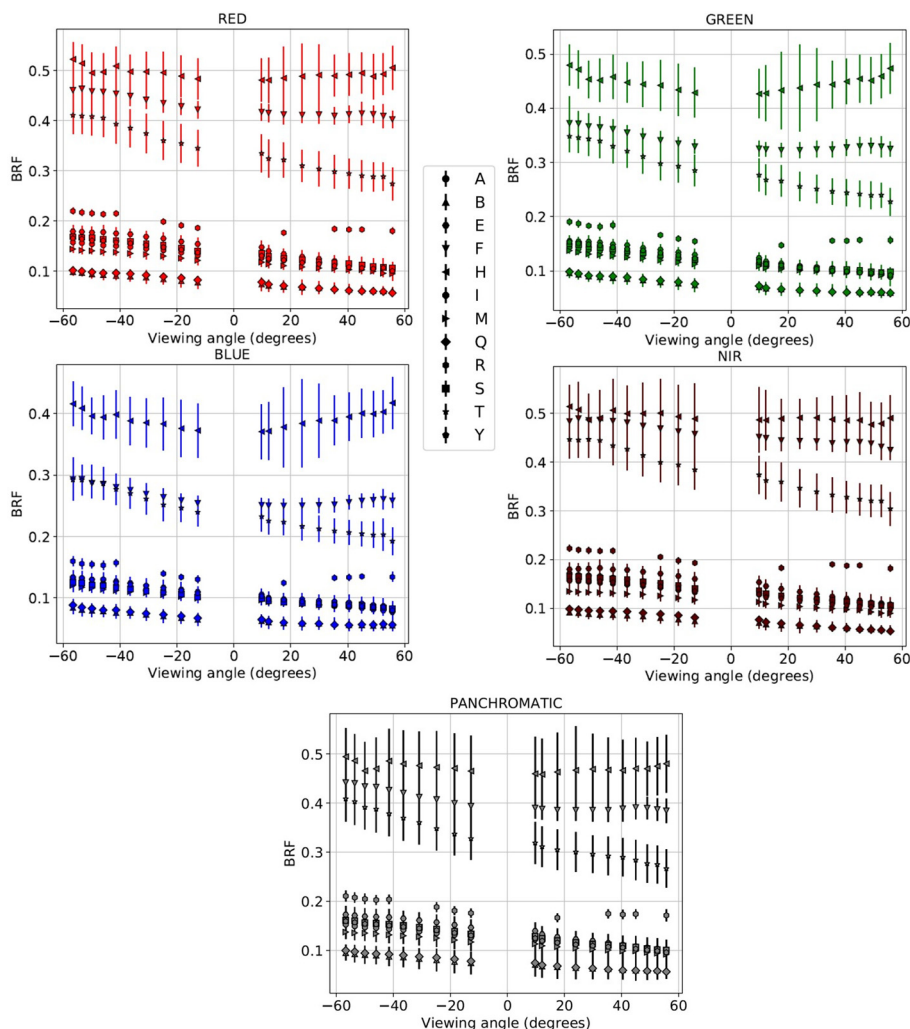


Fig. 11. Bidirectional reflectance factor (BRF) measured by Pleiades at twelve sites of the Asal-Ghoubbet rift in the four spectral bands and the panchromatic band of the sensor. By convention, the negative viewing angles correspond to azimuth angles ranging from 90° to 270° (Fig. 7b).

Table 2

Single scattering albedo w and photometric roughness $\bar{\theta}_H$ estimated by inversion of the Hapke model on multispectral (MS) and panchromatic (P) data. B, G, R and NIR stand for the blue, green, red and near-infrared bands of Pleiades, respectively.

Site	Sensor	Photometric roughness $\bar{\theta}_H$		Single scattering albedo w				
		P	MS	P	B	G	R	NIR
A	Pleiades	21.1 ± 16.1	21.9 ± 3.2	0.34 ± 0.17	0.26 ± 0.09	0.29 ± 0.11	0.33 ± 0.12	0.34 ± 0.12
	Chamelon	25.8 ± 6.8	24.7 ± 3.7	0.33 ± 0.15	0.28 ± 0.10	0.37 ± 0.12	0.37 ± 0.12	0.39 ± 0.12
B	Pleiades	28.5 ± 27.2	19.9 ± 16.2	0.30 ± 0.26	0.22 ± 0.09	0.24 ± 0.10	0.25 ± 0.10	0.24 ± 0.10
	Pleiades	33.7 ± 23.6	29.2 ± 6.5	0.46 ± 0.29	0.33 ± 0.12	0.38 ± 0.13	0.43 ± 0.14	0.44 ± 0.15
E	Chamelon	30.5 ± 7.3	30.7 ± 3.6	0.40 ± 0.18	0.31 ± 0.14	0.35 ± 0.15	0.43 ± 0.17	0.46 ± 0.17
	Pleiades	24.8 ± 15.8	27.1 ± 5.2	0.86 ± 0.13	0.43 ± 0.69	0.79 ± 0.13	0.88 ± 0.11	0.90 ± 0.09
F	Chamelon	19.5 ± 3.4	18.9 ± 2.4	0.93 ± 0.04	0.81 ± 0.04	0.88 ± 0.04	0.94 ± 0.03	0.95 ± 0.02
	Pleiades	14.8 ± 14.7	22.5 ± 14.5	0.89 ± 0.16	0.86 ± 0.13	0.90 ± 0.11	0.93 ± 0.10	0.93 ± 0.10
H	Chamelon	22.2 ± 5.7	21.6 ± 2.7	0.93 ± 0.05	0.88 ± 0.03	0.91 ± 0.03	0.94 ± 0.02	0.96 ± 0.02
	Pleiades	31.8 ± 22.0	30.6 ± 8.6	0.44 ± 0.28	0.35 ± 0.15	0.39 ± 0.16	0.43 ± 0.17	0.43 ± 0.17
M	Pleiades	32.1 ± 21.6	28.3 ± 4.5	0.40 ± 0.27	0.32 ± 0.12	0.35 ± 0.13	0.37 ± 0.13	0.36 ± 0.13
	Chamelon	40.8 ± 5.0	41.5 ± 3.5	0.28 ± 0.14	0.19 ± 0.06	0.21 ± 0.07	0.23 ± 0.07	0.23 ± 0.07
Q	Pleiades	26.4 ± 25.5	19.0 ± 13.5	0.26 ± 0.25	0.20 ± 0.08	0.22 ± 0.08	0.23 ± 0.09	0.23 ± 0.08
	Chamelon	22.0 ± 7.0	22.0 ± 3.6	0.21 ± 0.09	0.18 ± 0.07	0.19 ± 0.07	0.21 ± 0.08	0.21 ± 0.08
R	Pleiades	24.0 ± 15.7	25.7 ± 3.3	0.53 ± 0.23	0.42 ± 0.14	0.47 ± 0.14	0.54 ± 0.15	0.54 ± 0.15
	Chamelon	25.4 ± 6.30	25.5 ± 3.1	0.45 ± 0.17	0.40 ± 0.10	0.45 ± 0.11	0.51 ± 0.11	0.54 ± 0.12
S	Pleiades	29.4 ± 22.4	24.6 ± 4.9	0.41 ± 0.28	0.28 ± 0.10	0.33 ± 0.11	0.37 ± 0.11	0.36 ± 0.12
	Pleiades	26.4 ± 20.2	24.3 ± 14.2	0.74 ± 0.25	0.54 ± 0.17	0.61 ± 0.18	0.69 ± 0.18	0.73 ± 0.18
T	Chamelon	23.1 ± 5.3	22.1 ± 2.9	0.71 ± 0.18	0.58 ± 0.12	0.64 ± 0.12	0.73 ± 0.12	0.79 ± 0.12
	Pleiades	31.4 ± 23.7	24.4 ± 14.2	0.45 ± 0.28	0.32 ± 0.12	0.36 ± 0.14	0.38 ± 0.15	0.37 ± 0.15

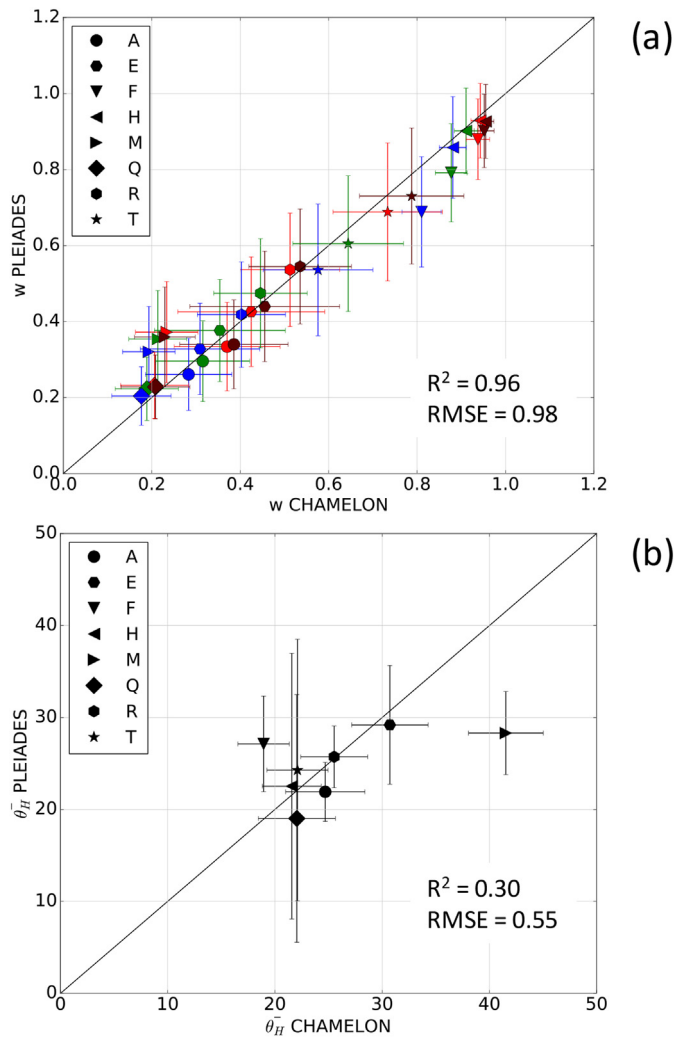


Fig. 12. Comparison of the photometric parameters estimated by Bayesian inversion of the Hapke model on the Pleiades and Chamelon data. (a) Single scattering albedo (blue, green, red and violet colors represent the four Pleiades spectral bands) and (b) Photometric roughness. (For interpretation of the references to color in this figure legend, the reader is referred to the web version of this article.)

porosity (P) and the opposition surge amplitude (B_0). By providing better observational constraints, the quality of the retrieval is generally improved. Without information on the uncertainty associated with the Chamelon observations, we fixed it to 10% of the observed values. Although between two and six complete BRFs are available in each site, we inverted the Hapke model on only one chosen on the basis of the stability of atmospheric conditions, the homogeneity of the surface, and the symmetry of the BRF with respect to the principal plane of the Sun. The Chamelon spectra were convoluted by the filter functions of the Pleiades sensor displayed in Fig. 3c to obtain spectrally homogeneous data. The retrieved values of $\bar{\theta}_H$, the parameter of interest, are gathered in Table 2 and Fig. 12. The single scattering albedo w is added to check consistency of the Chamelon-Pleiades cross-calibration.

On the one hand, the single scattering albedo of these sites covers the entire possible range of variation (from 0.21 to 0.93). The high values ($w > 0.8$) retrieved in sites F and H, the brightest surfaces, are close to values found over snowy surfaces or on icy satellites (Verbiscer et al., 2013). The synthetic tests showed a trend to overestimate this parameter, despite a good constraint brought by the a posteriori PDF. It is therefore likely that the true value of w is less than that estimated. However, the relative values are coherent: the sites made of blocks and

slabs of basaltic lava flows (B, M, and Q) are the darkest ($w < 0.4$), those made of granular deposits and boulders on sedimentary deposits (A, E, I, R, and S) are moderately bright ($0.4 < w < 0.6$), and those made of clay, salt and limestones (F, H, and T) are the brightest ($w > 0.6$). As for the spectral evolution of w , it agrees with previous studies (e.g., Johnson et al., 2006a, 2006b; Chappell et al., 2009; Wu et al., 2009; Sato et al., 2014). Fig. 12a shows the very good agreement between the single scattering albedo estimated from Pleiades and in situ Chamelon instrument. This is not surprising since the geometric correction parameter r has been chosen so as to minimize the residual error between the Chamelon and Pleiades data.

On the other hand, the retrieved values of $\bar{\theta}_H$ fluctuate between 15° and 35° . These values do not appear to reflect the relatively wide range and increasing macroscopic roughnesses observed in Fig. 2. For instance, the photometric roughness of site F might be expected much lower than that of site Q, which is not the case. Fig. 12b shows that the photometric roughness derived either from space or in situ coincides for almost all the sites, except for sites F and M. In the first case, the value estimated from the Pleiades data is larger, and in the second, it is lower. These discrepancies lie in a poor adjustment of the Hapke model illustrated by larger root-mean-square errors for sites F and M than for the other sites.

5. Discussion

The equivalence between the photometric roughness $\bar{\theta}_H$ estimated by inversion of the Hapke model and the mean roughness $\bar{\theta}$ measured in the field is not straightforward (Tables 1 and 2, Fig. 13). The former integrates all scales from the sub-millimeter scale to the decimeter scale, while the latter is derived from the slope distribution at the smallest DEM scale (~ 3 mm), assumed to be Gaussian. In most cases, the error bars are compatible with the hypothesis that $\bar{\theta}_H = \bar{\theta}$. Among the sites providing an error $< 25\%$, one can differentiate three groups:

- Sites A and S that are smooth surfaces consisting of centimetric grains, with similar mean roughness ($\bar{\theta} = 18.57^\circ$ for site A and $\bar{\theta} = 18.31^\circ$ for site S). The uncertainty on $\bar{\theta}_H$ is $< 16\%$.
- Sites E, I, R, and T that are made of centimetric to decimetric blocks. The a posteriori error on the photometric roughness is more significant, but the correspondence is very good for sites I, R and T. Sites E and R have a very close spatial structure (slag deposits on lacustrine sediments, Fig. 2) leading to similar $\bar{\theta}$ values. However, the difference between $\bar{\theta}_H$ and $\bar{\theta}$ for site E is slightly larger.
- Site H that corresponds to the salt lake with a granular structure and optical properties deviating from those of rocky terrain. The uncertainty on the $\bar{\theta}_H$ estimate is very large.

The retrieval is poor for sites B (ropy pahoehoe lava), Q (basalt porphyry lava), F (clay deposits), Y (hyaloclastic projections) and M (cracked lava crust). The estimated photometric roughnesses is similar for sites B and Q that are comparable in terms of visual aspect of surface roughness. As far as the Chamelon is concerned, the photometric roughness and the mean roughness measured in the field agree well for moderate roughness (sites A, E, H, R, and T) with a relative error of 17.2%. The absence of correlation for sites F, M and Q still comes out.

The sources of discrepancy are difficult to identify. The Orfeo ToolBox used for the atmospheric correction assumes that the surface is Lambertian, which is naturally wrong in nature and may affect the calculation of the reflectance (e.g., Lyasputin, 1999; Li et al., 2010; Ceamanos et al., 2013). The effect of the local topography can be also accounted for but we ignored it here because the surfaces studied are nearly flat. Li et al. (2012) highlighted the effectiveness of these two corrections on Landsat temporal data. Therefore, it is likely that an approximate atmospheric correction based on Lambertian assumptions has an impact on the estimation of surface roughness, especially at grazing viewing angles.

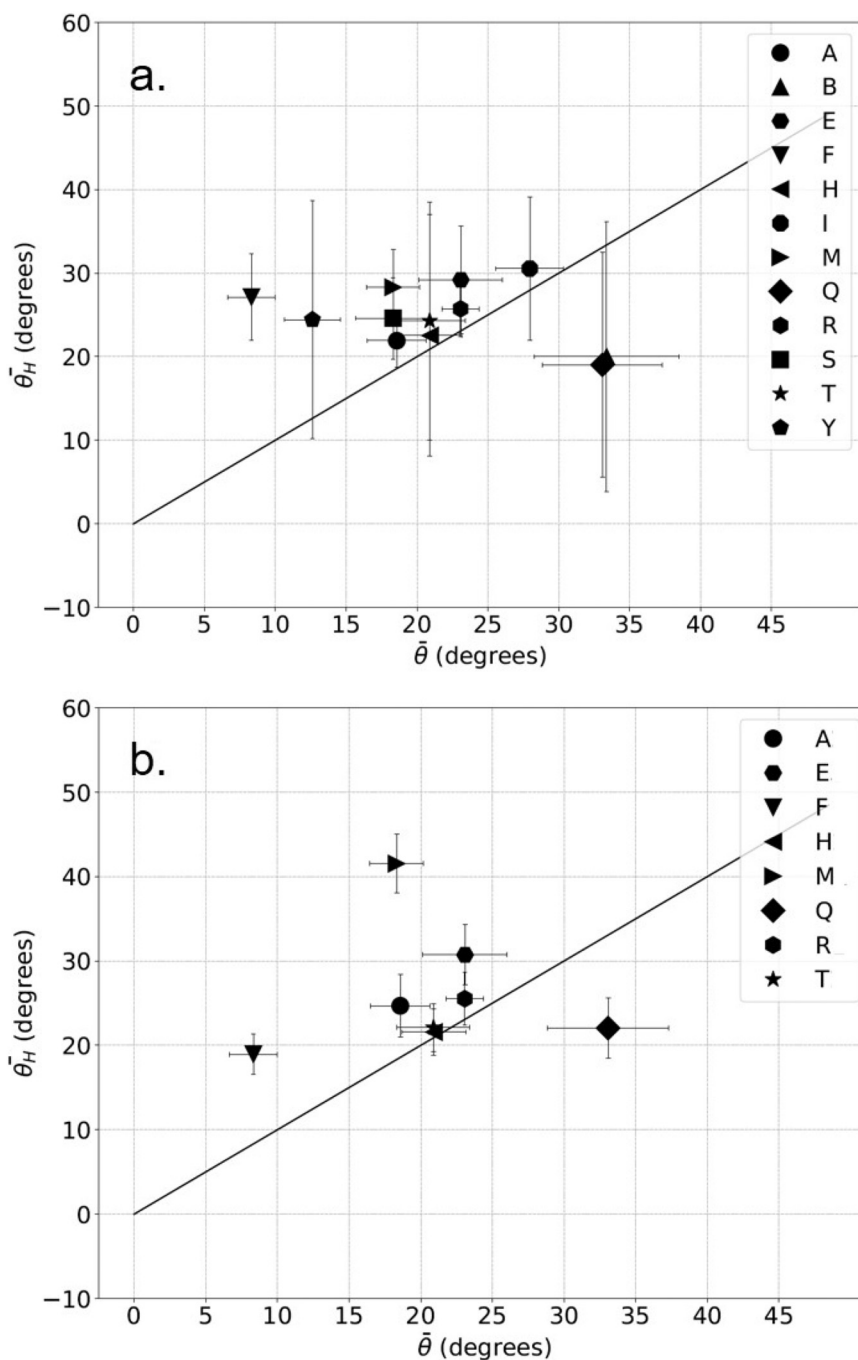


Fig. 13. Estimated photometric roughness $\bar{\theta}_H$ as a function of the measured mean roughness $\bar{\theta}$ for 12 sites (see Fig. 2) from (a) Pleiades data and (b) Chamelon data.

The estimation of surface roughness through photometric roughness seems to be satisfactory on surfaces displaying granular structures, the size of which is greater than a centimeter, or small blocks. In the case of finer-grained surfaces or more complex structures (slabs, fractures, depressions), the Hapke model fits the observations but the roughness estimates are biased. The performance of the inversion may be poor if the surface departs too much from the hypotheses of the Hapke model. Moreover, the photometric roughness that measures shading at the particle scale is supposed to also depend on the transparency of the particles and their scattering behavior (e.g., Shepard and Campbell, 1998; Cord et al., 2003; Pilorget et al., 2016). Finally, the Hapke model considers a collimated incident light while the atmospheric scattering makes the sun light a spread source for terrestrial surfaces. This tends to reduce the shadowing on the surface and to underestimate the

photometric roughness. Note that the part of the reflectance due to diffuse light is still a pending question on soils, while it has been quantified for a long time on vegetation. Last but not least, Labarre et al. (2017) showed that the photometric roughness was controlled by the smallest scales of the surface. Thus, it is likely that this parameter is sensitive to scales smaller than the scale of the DEMs produced in this study for the computation of the mean roughness parameter. This would result in an underestimation of $\bar{\theta}$, in particular for the smoothest surfaces.

6. Conclusion

We have investigated the capacity of the Hapke model to retrieve the surface roughness of bare soils from multiangular reflectance data.

This model is indeed commonly used in planetary science even if its validation is still an open issue. We aimed at coupling in situ measurements on bare soils with remote multiangular observations at high resolution to address this issue or show the potentials and limits of these data and method. Because of its agility and spatial resolution, the Pleiades satellite was able to measure angular reflectance of natural surfaces of reduced extend and wide diversity, from space, from a large number of viewing angles, which, with a few exceptions is unique on Earth remote sensing. If performant this model would provide a new physical description of bare soils with many derived applications.

For the first time we measured the topography of large areas ($\sim 20 \text{ m} \times 20 \text{ m}$) at the millimeter scale, determined their surface roughness defined as the mean slope angle, and tried to relate the photometric roughness as derived from to multi-angular optical data acquired in the field of from space. We showed that the atmospheric correction is critical to estimate surface roughness, due to the strong influence of aerosols but also of the adjacency effect on the shape and amplitude of the bidirectional reflectance. Part of this issue was solved by cross-calibrating remote and in situ observations in R, G, B and IR bands. We emphasized that the Lambertian assumption enclosed in the software used for the atmospheric correction may have an impact on the results. A Bayesian inversion of the Hapke model was conducted to cope with the non-linearity of the model and to assess the uncertainties associated with parameter estimation. Two approaches were explored: the first one consisting of a simultaneous inversion on the four Pleiades bands, assuming that the single scattering albedo is the only wavelength-dependent parameter, and the second one consisting of an inversion on the panchromatic band. Results were found better in the first

case, with greatly reduced uncertainties on the parameters, because of better observational constraints.

This study revealed that the coherence between the photometric roughness $\bar{\sigma}_H$ and the mean roughness $\bar{\tau}$ was good for moderately rough surfaces presenting homogeneous granular structures, but poor for solid floor areas or highly rough surfaces presenting more complex structures (slabs, hollows, fractures), which do not fit Hapke model hypotheses. This article is the result of an exploratory work and provides a framework to scientists wishing to estimate surface roughness using optical remote sensing. Other experiments will be required at different scales, including the topographic one, before we totally understand the determinism of soil bidirectional reflectance.

Acknowledgments

The PhD thesis of Sébastien Labarre was funded by the Direction générale de l'armement (DGA) and by the Commissariat à l'énergie atomique et aux énergies alternatives (CEA). Field data were acquired in the frame of the CAROLInA (*Characterization of Multi-Scale Roughness using Optical Imagery*) project funded by CNES. The authors would like to thank Sophie Lachéradé (CNES) and Claire Tinel (CNES) who enabled us to acquire the Pleiades images, Jean-Bernard de Chabalière (IPGP) who guided part of the team in the Asal-Ghoubbet rift during the exploratory mission in April 2015, Héléne Robic (IPGP), Michel Diament (IPGP) and Yann Klinger (IGGP) for their invaluable help, the CERD team who provided us logistical assistance on the ground. Fig. 1 contains modified Copernicus Sentinel data 2018, processed by ESA.

Appendix A. Calibration and atmospheric corrections

The calibration and atmospheric correction of the Pleiades images follow the four steps illustrated in Fig. 8. First the numerical value X_k recorded in band k is converted to spectral radiance [$\text{W} \cdot \text{m}^{-2} \cdot \text{sr}^{-1} \cdot \mu\text{m}^{-1}$] according to

$$I_{k,TOA} = \frac{X_k}{\alpha_k} + \beta_k \quad (\text{A1})$$

where $I_{k,TOA}$ is the radiance measured at the top of the atmosphere, α_k is the absolute calibration gain, and β_k is the absolute calibration bias. These two parameters are contained in the metadata. The radiance value can be then converted into a TOA reflectance factor:

$$\rho_{k,TOA} = \frac{\pi I_{k,TOA} d_0^2}{J_{k,i} \mu_0} \quad (\text{A2})$$

with $J_{k,i}$ the solar illumination at the upper limit of the atmosphere for the Earth-Sun distance d_0 expressed in astronomical units, at the date of acquisition. In order to calculate the surface reflectance, one needs to provide the atmospheric pressure P_a [hPa], the water vapor content U_{H_2O} [$\text{g} \cdot \text{cm}^{-2}$], the ozone content U_{O_3} [DU], the aerosol optical thickness τ_a at 550 nm, a predefined aerosol model (desert) to determine the aerosol phase function P_A and the single scattering albedo ω_0 , as well as sensor intrinsic parameters (solar and viewing zenith and azimuth angles, acquisition date, sensor spectral response at a given wavelength).

Gases and aerosols are the two major atmospheric constituents causing the extinction of solar radiation by absorption or scattering. According to Vermote et al. (1997), the TOA reflectance factor of a uniform and Lambertian surface illuminated with an incidence angle i and observed at a viewing angle e , is written as

$$\rho_{TOA} = \rho_{atm} + T(i)T(e) \frac{\rho_t}{1 - \rho_t S} \quad (\text{A3})$$

with ρ_{atm} the intrinsic atmospheric reflectance factor, $T(i)$ and $T(e)$ the total atmospheric transmittances in the illumination (i) and viewing (e) directions, ρ_t the reflectance factor of the target, and S the atmospheric spherical albedo. Taking explicitly into account absorption by water vapor and ozone, the TOA reflectance factor ρ_{TOA} at a given wavelength becomes:

$$\rho_{TOA}(i, e, \phi, P_a, \tau_a, \omega_0, P_A, U_{H_2O}, U_{O_3}) = T(i, e, \phi, P_a, U_{O_3}) \left[\rho_{atm}(i, e, \phi, P_a, \tau_a, \omega_0, P_A, U_{H_2O}) + T_{atm}(i, e, \phi, P_a, \tau_a, \omega_0, P_A) \frac{\rho_t}{1 - \rho_t S(P_a, \tau_a, \omega_0, P_A)} T_{H_2O}(i, e, U_{H_2O}) \right] \quad (\text{A4})$$

with U_{H_2O} the total atmospheric water vapor content [$\text{g} \cdot \text{cm}^{-2}$], U_{O_3} the total column ozone content [DU], T_{H_2O} the transmittance of atmospheric water vapor, T the transmittance of all other gases, T_{atm} the total atmospheric transmittance, $\phi = \phi_e - \phi_i$ the relative azimuth angle, P_a the atmospheric pressure [hPa], τ_a the aerosol optical thickness, ω_0 the aerosol single scattering albedo, and P_A the aerosol phase function.

To take into account the nonuniformity of the surface, the average reflectance $\langle \rho \rangle$ of the pixels surrounding the target pixel is computed as (Vermote et al., 1997):

$$\langle \rho \rangle = \int_0^{2\pi} \int_0^{\infty} \rho'(r, \psi) F(r) d\psi dr \quad (\text{A5})$$

with $F(r)$ the environmental function (probability that a photon incident on the target be scattered and impacts the surface within a circle of radius r around the target center) and $\rho'(r, \psi)$ the surface reflectance in polar coordinates. The boundary conditions are $F(0) = 0$ and $F(\infty) = 1$. $F(r)$ is a complex function of the molecule and aerosol phase function, their optical thickness and vertical distribution. Their contribution can be taken into account separately:

$$F(r) = \frac{t_d^R(e) F_R(r) + t_d^A(e) F_A(r)}{t_d(e)} \quad (\text{A6})$$

with $t_d^R(\mu)$ and $t_d^A(\mu)$ the diffuse transmission factors for molecules and aerosols. Finally, the surface reflectance ρ_c is expressed as

$$\rho_c = \frac{\rho_i T(e) - \langle \rho \rangle t_d(e)}{e^{-\tau/\mu}} \quad (\text{A7})$$

where $t_d(e)$ is the diffuse transmittance factor in the viewing direction, τ is the atmospheric optical thickness and $\mu = \cos e$.

Appendix B. Shadowing function

The shadowing function used in Eq. (2) is detailed in Hapke (2012). There are two different ways of calculating it:

$$S(i, e, g, \overline{\theta_H})_{i \leq e} = \frac{\mu_e \mu_0}{\eta(e) \eta(i)} \frac{\chi(\overline{\theta_H})}{1 - f(\phi) + f(\phi) \chi(\overline{\theta_H}) [\mu_0 / \eta(i)]} \quad (\text{B1})$$

$$S(i, e, g, \overline{\theta_H})_{i > e} = \frac{\mu_e \mu_0}{\eta(e) \eta(i)} \frac{\chi(\overline{\theta_H})}{1 - f(\phi) + f(\phi) \chi(\overline{\theta_H}) [\mu / \eta(e)]} \quad (\text{B2})$$

with i and e are the illumination and viewing angles, $\overline{\theta_H}$ is the photometric roughness, $\mu_0 = \cos i$, $\mu = \cos e$, and μ_e is the cosine of the effective viewing angle. The functions χ , η and f are written as

$$\chi(\overline{\theta_H}) = \frac{1}{1 + \pi \tan^2(\overline{\theta_H})} \quad (\text{B3})$$

$$\eta(x) = \chi(\overline{\theta_H}) \left[\cos(x) + \sin(x) \tan(\overline{\theta_H}) \frac{E_2(x)}{2 - E_1(x)} \right] \quad (\text{B4})$$

$$f(\phi) = \exp\left(-2 \tan\left(\frac{\phi}{2}\right)\right) \quad (\text{B5})$$

with

$$E_1(x) = \exp\left(-\frac{2}{\pi} \cot(\overline{\theta_H}) \cot(x)\right) \quad (\text{B6})$$

$$E_2(x) = \exp\left(-\frac{1}{\pi} \cot^2(\overline{\theta_H}) \cot^2(x)\right) \quad (\text{B7})$$

Appendix C. Supplementary data

Supplementary data associated with this article can be found in the online version, at <https://doi.org/10.1016/j.rse.2019.02.014>. These data include the Google map of the most important areas described in this article.

References

- Antonenko, I., Osinski, G.R., 2010. In: Automated Detection of Basalt Spectra in Clementine Lunar Data. Proc. 41st Lunar and Planetary Science Conference. pp. 26–27.
- Bachmann, C.M., Abelev, A., Montes, M.J., Philpot, W., Gray, D., Doctor, K.Z., Fusina, R.A., Mattis, G., Chen, W., Noble, S.D., Coburn, C., Corl, T., Slomer, L., Nichols, C.R., van Roggen, E., Hughes, R.J., Carr, S., Kharabash, S., Brady, A., Vermillion, M., 2016. Flexible field goniometer system: the goniometer for outdoor portable hyperspectral earth reflectance. *J. Appl. Remote. Sens.* 10 (3), 036012.
- Beck, P., Pommerol, A., Thomas, N., Schmitt, B., Moynier, F., Barrat, J.A., 2012. Photometry of meteorites. *Icarus* 218 (1), 364–377.
- Bretar, F., Arab-Sedze, M., Champion, J., Pierrot-Deseilligny, M., Heggy, E., Jacquemoud, S., 2013. An advanced photogrammetric method to measure surface roughness: application to volcanic terrains in the Piton de la Fournaise, Reunion Island. *Remote Sens. Environ.* 135, 1–11.
- Caminiti, A.M., 2000. Le fossé d'Asal et le lac Abhé. Deux sites géologiques exceptionnels en République de Djibouti. Editions Couleur Locale (128 pp.).
- Ceamanos, X., Douté, S., Fernando, J., Schmidt, F., Pinet, P., Lyapustin, A., 2013. Surface reflectance of Mars observed by CRISM/MRO: 1. Multi-angle Approach for Retrieval of Surface Reflectance from CRISM observations (MARS-ReCO). *J. Geophys. Res. Planets* 118 (3), 514–533.
- Chappell, A., Zobeck, T.M., Brunner, G., 2006. Using bi-directional soil spectral reflectance to model soil surface changes induced by rainfall and wind-tunnel abrasion. *Remote Sens. Environ.* 102 (3–4), 328–343.
- Chappell, A., Leys, J.F., McTainsh, G.H., Strong, C., Zobeck, T.M., 2009. Simulating Multi-angle Imaging Spectro-Radiometer (MISR) sampling and retrieval of soil surface roughness and composition changes using a bi-directional soil spectral reflectance model. In: Roeder, A., Hill, J. (Eds.), Recent Advances in Remote Sensing and Geoinformation Processing for Land Degradation Assessment. Taylor & Francis, pp. 243–259.
- Cierniewski, J., 1987. A model for soil surface roughness influence on the spectral response of bare soil in the visible and near-infrared range. *Remote Sens. Environ.* 23 (1), 97–115.
- Cord, A., Pinet, P., Daydou, Y., Chevrel, S., 2003. Planetary regolith surface analogs: optimized determination of Hapke parameters using multi-angular spectro-imaging laboratory data. *Icarus* 165 (2), 414–427.
- Despan, D., Bedidi, A., Cerville, B., 1999. Bidirectional reflectance of rough bare soil surfaces. *Geophys. Res. Lett.* 26 (17), 2777–2780.
- Doctor, K.Z., Bachmann, C.M., Gray, D.J., Montes, M.J., Fusina, R.A., 2015. Wavelength dependence of the bidirectional reflectance distribution function (BRDF) of beach sands. *Appl. Opt.* 54 (31), F243.
- Fernando, J., Schmidt, F., Ceamanos, X., Pinet, P., Douté, S., Daydou, Y., 2013. Surface reflectance of Mars observed by CRISM/MRO: 2. Estimation of surface photometric properties in Gusev Crater and Meridiani Planum. *J. Geophys. Res. Planets* 118,

- 534–559.
- Fernando, J., Schmidt, F., Pilorget, C., Pinet, P., Ceamanos, X., Douté, S., Daydou, Y., Costard, F., 2015. Characterization and mapping of surface physical properties of Mars from CRISM multi-angular data: application to Gusev Crater and Meridiani Planum. *Icarus* 253, 271–295.
- Furey, J., 2016. Laboratory goniometer approach for spectral polarimetric directionality. In: Chenault, D.B., Goldstein, D.H. (Eds.), *Proc. Polarization: Measurement, Analysis, and Remote Sensing XII*. vol. 9853. SPIE, Baltimore, MD, USA, pp. 985301 17 April 2016.
- Gilliot, J.M., Vaudour, E., Michelin, J., 2017. Soil surface roughness measurement: a new fully automatic photogrammetric approach applied to agricultural bare fields. *Comput. Electron. Agric.* 134, 63–78.
- Gleyzes, M.A., Perret, L., Kubik, P., 2012. Pleiades system architecture and main performances. In: *International Archives of the Photogrammetry, Remote Sensing and Spatial Information Sciences, XXII ISPRS Congress, 25 August–01 September 2012, Melbourne, Australia*. vol. XXXIX-B1. pp. 537–542.
- Gunderson, K., Thomas, N., Whitby, J.A., 2006. First measurements with the Physikalisches Institut Radiometric Experiment (PHIRE). *Planet. Space Sci.* 54 (11), 1046–1056.
- Hapke, B., 1981. Bidirectional reflectance spectroscopy: 1. Theory. *J. Geophys. Res. Solid Earth* 86 (B4), 3039–3054.
- Hapke, B., 1984. Bidirectional reflectance spectroscopy: 3. Correction for macroscopic roughness. *Icarus* 59 (1), 41–59.
- Hapke, B., 2008. Bidirectional reflectance spectroscopy: 6. Effects of porosity. *Icarus* 195 (2), 918–926.
- Hapke, B., 2012. *Theory of Reflectance and Emittance Spectroscopy*. Cambridge University Press (528 pages).
- Harms, J.D., Bachmann, C.M., Faulring, J.W., Ruiz Torres, A.J., 2016. A next generation field-portable goniometer system. In: Velez-Reyes, M., Messinger, D.W. (Eds.), *Proc. Algorithms and Technologies for Multispectral, Hyperspectral, and Ultraspectral Imagery XXII*. vol. 9840. SPIE, Baltimore, MD, USA, pp. 98400J 17 April 2016.
- Helfenstein, P., Shepard, M.K., 2011. Testing the Hapke photometric model: improved inversion and the porosity correction. *Icarus* 215 (1), 83–100.
- Irons, J.R., Campbell, G.S., Norman, J.M., Graham, D.W., Kovalick, W.M., 1992. Prediction and measurement of soil bidirectional reflectance. *IEEE Trans. Geosci. Remote Sens.* 30 (2), 249–260.
- Jacquemoud, S., Baret, F., Hanocq, J.F., 1992. Modeling spectral and bidirectional soil reflectance. *Remote Sens. Environ.* 41 (2–3), 123–132.
- Johnson, J.R., Grundy, W.M., Lemmon, M.T., Bell, J.F., Johnson, M.J., Deen, R., Arvidson, R.E., Farrand, W.H., Guinness, E.A., Hayes, A.G., Herkenhoff, K.E., Seelos, F., Soderblom, J., Squyres, S., 2006a. Spectrophotometric properties of materials observed by Pancam on the Mars Exploration Rovers: 1. Spirit. *J. Geophys. Res. Planets* 111 (E2), E02S14.
- Johnson, J.R., Grundy, W.M., Lemmon, M.T., Bell, J.F., Johnson, M.J., Deen, R., Arvidson, R.E., Farrand, W.H., Guinness, E.A., Hayes, A.G., Herkenhoff, K.E., Seelos, F., Soderblom, J., Squyres, S., 2006b. Spectrophotometric properties of materials observed by Pancam on the Mars Exploration Rovers: 2. Opportunity. *J. Geophys. Res. Planets* 111 (E12), E12S16.
- Johnson, J.R., Shepard, M.K., Grundy, W.M., Paige, D.A., Foote, E.J., 2013. Spectrogoniometry and modeling of martian and lunar analog samples and Apollo soils. *Icarus* 223 (1), 383–406.
- Labarre, S., Ferrari, C., Jacquemoud, S., 2017. Surface roughness retrieval by inversion of the Hapke model: a multiscale approach. *Icarus* 290, 63–80.
- Lachérade, S., Fourest, S., Gamet, P., Lebègue, L., 2012. Pleiades absolute calibration: inflight calibration sites and methodology. In: *ISPRS International Archives of the Photogrammetry, Remote Sensing and Spatial Information Sciences*. XXXIX-B1. pp. 549–554.
- Li, F., Lymburner, L., Mueller, N., Tan, P., Islam, A., Jupp, D.L.B., Reddy, S., 2010. An evaluation of the use of atmospheric and BRDF correction to standardize Landsat data. *IEEE J. Sel. Top. Appl. Earth Obs. Remote Sens.* 3 (3), 257–270.
- Li, F., Jupp, D.L.B., Thankappan, M., Lymburner, L., Mueller, N., Lewis, A., Held, A., 2012. A physics-based atmospheric and BRDF correction for Landsat data over mountainous terrain. *Remote Sens. Environ.* 124, 756–770.
- Lumme, K., Bowell, E., 1981. Radiative transfer in the surfaces of atmosphereless bodies. I. Theory. *Astron. J.* 86 (11), 1694–1721.
- Lyasputin, A.I., 1999. Atmospheric and geometrical effects on land surface albedo. *J. Geophys. Res. Atmos.* 104 (D4), 4127–4143.
- Patil, A., 2010. PyMC: Bayesian stochastic modelling in Python. *J. Stat. Softw.* 35 (4), 1–81.
- Pierrot-Deseilligny, M., Paparoditis, N., 2006. A multiresolution and optimization-based image matching approach: an application to surface reconstruction from SPOT5-HRS stereo imagery. In: *Proc. Topographic Mapping from Space (with Special Emphasis on Small Satellites)*, 14–16 February 2006. vol. XXXVI-1/W41 ISPRS Archives, Ankara, Turkey (5 pp.).
- Pilorget, C., Fernando, J., Ehlmann, B.L., Schmidt, F., Hiroi, T., 2016. Wavelength dependence of scattering properties in the VIS-NIR and links with grain-scale physical and compositional properties. *Icarus* 267, 296–314.
- Pinty, B., Verstraete, M.M., Dickinson, R.E., 1989. A physical model for predicting bidirectional reflectances over bare soil. *Remote Sens. Environ.* 27 (3), 273–288.
- Pinzuti, P., Humler, E., Manighetti, I., Gaudemer, Y., 2013. Petrological constraints on melt generation beneath the Asal Rift (Djibouti) using quaternary basalts. *Geochem. Geophys. Geosyst.* 14 (8), 2932–2953.
- Pommerol, A., Thomas, N., Jost, B., Beck, P., Okubo, C., McEwen, A.S., 2013. Photometric properties of Mars soils analogs. *J. Geophys. Res. Planets* 118 (10), 2045–2072.
- Rupnik, E., Daakir, M., Pierrot-Deseilligny, M., 2017. MicMac – a free, open-source solution for photogrammetry. In: *Open Geospatial Data, Software and Standards*. 2. pp. 14.
- Rupnik, E., Pierrot-Deseilligny, M., Delorme, A., 2018. 3D reconstruction from multi-view VHR-satellite images in MicMac. *ISPRS J. Photogramm. Remote Sens.* 139, 201–211.
- Sandmeier, S.R., 2000. Acquisition of bidirectional reflectance factor data with field goniometers. *Remote Sens. Environ.* 73 (3), 257–269.
- Sato, H., Robinson, M.S., Hapke, B., Denevi, B.W., Boyd, A.K., 2014. Resolved Hapke parameter maps of the moon. *J. Geophys. Res. Planets* 119 (8), 1775–1805.
- Schaepman-Strub, G., Schaepman, M.E., Painter, T.H., Dangel, S., Martonchik, J.V., 2006. Reflectance quantities in optical remote sensing—definitions and case studies. *Remote Sens. Environ.* 103 (1), 27–42.
- Schmidt, F., Fernando, J., 2015. Realistic uncertainties on Hapke model parameters from photometric measurement. *Icarus* 260, 73–93.
- Shepard, M.K., Campbell, B.A., 1998. Shadows on a planetary surface and implications for photometric roughness. *Icarus* 134 (2), 279–291.
- Shepard, M.K., Helfenstein, P., 2007. A test of the Hapke photometric model. *J. Geophys. Res. Planets* 112 (E3), E03001.
- Shepard, M.K., Helfenstein, P., 2011. A laboratory study of the bidirectional reflectance from particulate samples. *Icarus* 215 (2), 526–533.
- Shkuratov, Y., Helfenstein, P., 2001. The opposition effect and the quasi-fractal structure of regolith: I. Theory. *Icarus* 152 (1), 96–116.
- Souchon, A.L., Pinet, P.C., Chevrel, S.D., Daydou, Y.H., Baratoux, D., Kurita, K., Shepard, M.K., Helfenstein, P., 2011. An experimental study of Hapke's modeling of natural granular surface samples. *Icarus* 215 (1), 313–331.
- Staid, M., 2000. Integrated spectral analysis of Mare soils and craters: applications to eastern nearside basalts. *Icarus* 145 (1), 122–139.
- Stieltjes, L., 1980. *Carte géologique du rift d'Asal 1/50 000 (Dépression Afar, est-africain. République de Djibouti)*. CNRS Editions, Paris.
- Verbiscer, A.J., Helfenstein, P., Buratti, B.J., 2013. Photometric properties of Solar System ices. In: Gudipati, M.S., Castillo-Rogez, J. (Eds.), *The Science of Solar System Ices*. Springer, pp. 47–72.
- Vermote, E., Tanré, D., Deuzé, J.L., Herman, M., Morcrette, J.J., 1997. Second simulation of the satellite signal in the solar spectrum (6S): an overview. *IEEE Trans. Geosci. Remote Sens.* 35, 675–686.
- Vincendon, M., 2013. Mars surface phase function constrained by orbital observations. *Planet. Space Sci.* 76 (1), 87–95.
- Wu, Y., Gong, P., Liu, Q., Chappell, A., 2009. Retrieving photometric properties of desert surfaces in China using the Hapke model and MISR data. *Remote Sens. Environ.* 113 (1), 213–223.